Proc. of the 9th International Symposium on Geotechnical Safety and Risk (ISGSR)
Edited by Zhongqiang Liu, Jian Dai and Kate Robinson
Published by Research Publishing, Singapore. ©2025 The Author(s), CC-BY 4.0 licence.
doi: 10.3850/GRF-25280825_isgsr-231-P267-cd

LANDSLIDE DEFORMATION AND TEMPORAL PREDICTION OF SLOPE FAILURE IN HIMALAYAN TERRAIN USING INSAR TIME SERIES.

Akshay Raj Manocha[1,2,]

1 University of Silesia in Katowice, Institute of Earth Sciences, Sosnowiec, Poland
2 International Environmental Doctoral School, University of Silesia in Katowice, Sosnowiec, Poland

Landslides pose a significant threat in mountainous regions, causing infrastructure damage and loss of life. Traditional methods for investigating landslides are often time-consuming and space-limited. Interferometric Synthetic Aperture Radar (InSAR) offers a powerful new tool for both detecting and monitoring landslides. This study focuses on the Sataun landslide, located along National Highway-72 (NH-72) in the Sirmaur district of Himachal Pradesh, India. Geological analysis revealed the landslide area consists mainly of Middle Siwalik sandstones, heavily fractured due to the interaction of the Sirmauri Tal Fault zone and the Malgi Fault. The Three Major faults with a high risk of landslides were identified, with a major failure occurring on October 9th, 2019. The study proposes a methodology for measuring displacement over time and predicting future slope failures in hilly areas. This method utilizes LiCSBAS, an open-source tool for analyzing time series data from Sentinel-1 SAR (Synthetic Aperture Radar) satellites. LiCSBAS enables users to easily obtain InSAR time series and velocity estimates wherever sufficient LiCSAR products are available. LiCSBAS simplifies InSAR time series analysis, requiring minimal user input. By analyzing the displacement time series derived from radar data, the method can identify reliable locations for persistent scatterers. This allows for the prediction of slope failure initiation months before the actual event. The study employs inverse velocity and modifies inverse velocity methods to identify potential time windows for slope failure. These methods showed good agreement between the predicted failure dates and the observed deformation patterns in the time series data. This study highlights the potential of such predictive methodologies for developing early warning systems for landslides. Such systems are crucial for mitigating the devastating impacts of landslides in mountainous regions. This emphasizes the importance of continuous monitoring to prevent future landslide events.

Keyword: Landslide, InSAR, LiCSBAS, Deformation

1. Introduction:

The Himalaya emerged as a young mountain range, originating from a continental collision approximately 56 million years ago (Jain 2014). Landslides in these types of terrains are sudden hazards causedmostly due to slope failures. They pose significant threats to human lives, property, and the economy disrupting road transportation and communication links. Our study focuses on the sataun landslide which is situated in the Sirmaur district of Himachal Pradesh, located in the north-west Himalayas. Erroneous grading of slopes and the construction of roads and structures without lateral support are the primary causes of slope collapse in the Sirmaur area along National Highway (NH) 707.We aim to detection of land subsidence to understand the deformation mechanism using Synthetic Aperture Radar (SAR) Interferometry (InSAR)on the Sataun landslide, showcasing the capability of Looking into Continents from Space with Synthetic Aperture Radar (LiCSAR)technique its effects, availability and Limitations in analyzing small-scale time-series deformations and predicting the timing of slope failure. A massive landslide near the Sataun city on the NH 707 was firstly recorded date back to 1956, then in 1998 (Awasti 1966, Srikantia and Bhargawa 1998) and thereafter followed by 9th October 2019, another failure on 1stAugust 2020 (Thakur et. al., 2023). This landslide was recently active post monsoon 2022. This recent incident marked one of the extensively investigated and monitored active landslides in the north-western Himalayan region. This landslide had affected the near Sataun town which is the hub of limestone market. It did major damage to the limestone market near the sataun town next to the river(Das et al., 2011).

In this study we have used theCenter of Observation and modelling of earthquakes, volcanoes and tectonics (COMET) UK team developed LiCSAR system (Lazeckyet. al. 2020) This system generates Sentinel-1 interferograms within a network optimized for processing through Small Baselines (SB) (Berardino et. al., 2002) inversion techniques and shares the outputs as open data to benefit the broader scientific community, particularly in advancing understanding of solid Earth processes.These interferograms, along with complementary products like Generic Atmospheric Correction Online Service (GACOS)(Yu C et al. 2018) atmospheric phase screen models, can be seamlessly integrated into the custom-built LiCSAR method for small Baselines (LiCSBAS) time series tool (Morishita et. al. 2010, 2020) to measure surface deformation over extended periods. The SB (Berardinoet al., 2002) technique, along with its variant NSBAS (Schmidt and Burgmann2003), forms the foundation of LiCSBAS (https://www.github.com/comet-licsar/LiCSBAS) and provides an accurate method for deriving displacement information using SAR interferometry (InSAR). However, the reliability of these results depends on the quality of

the source data, specifically the set of unwrapped interferograms that comprise a redundant network. In this study we have used the open-source InSAR time series analysis package that facilitates nearly automatic processing of time series using LiCSBAS products (Morishita et al., 2020) to LiCSAR products to derive deformation time series and velocities for major landslide area of Sirmaur district of Himachal Pradesh. The analysis, performed with predefined parameters, identified numerous subsidence signals and other deformation patterns with varying spatial and temporal characteristics. The processed datasets—including deformation time series, velocities, and noise indices—are publicly available in an open repository(Morishita et. al. 2010, 2020).

2. Study Area

The Himalaya spans the northern portion of the Indian subcontinent and is made up of a range of rock types and structural discontinuities that are prone to landslides. The steep landscape of India's northwest Himalaya region makes it very susceptible to landslides(Thakur et. al., 2023).Sataun is a town situated on the left bank of the Giri River in the Himachal Pradesh, India, Sirmaur district (Fig 1). The Sataun area is located near the Main Boundary Thrust (MBT) zone, which is where the Lesser Himalaya pushes aside the Sub-Himalayan Siwalik Group. The Sataun area is limited tectonically by the MBT, which is home to several cross-cutting active faults (Fig. 1). The MBT is locally termed as the Krol Thrust (Karunakaran and Rao 1979; Raiverman et al. 1994; Powers et al. 1998) towards the north and the Nahan Thrust (NT) towards the south (Fig. 1).

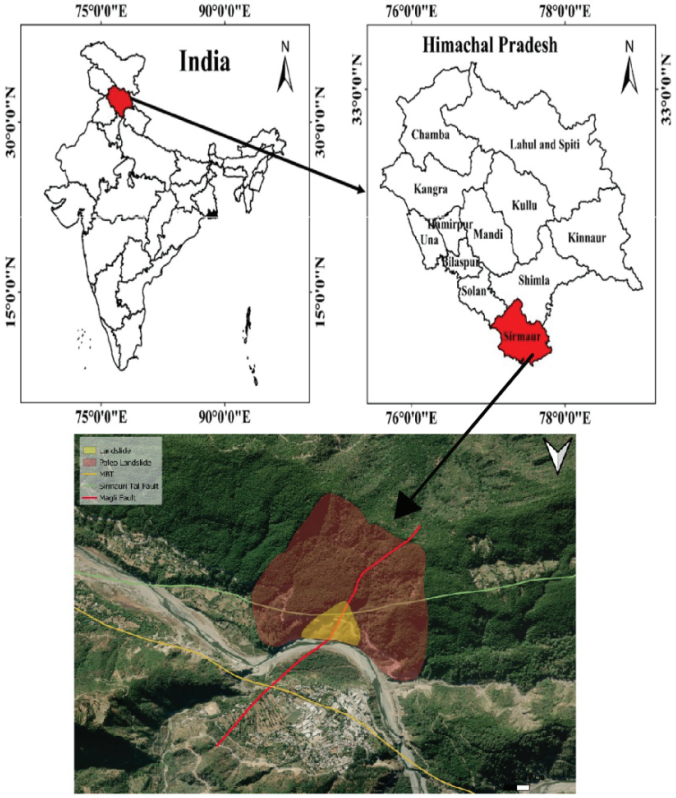


Fig 1: This figure shows the location of our study area region. A landslide event occurred near NH 707 which is known as Sataun in Sirmaur District.The figure also depicts the major thrust and fault passing through this region.

In terms of tectonics and lithology, the Sataun area is quite complex. This sector features a variety of lithologies, from Proterozoic limestones to alluvium that was recently deposited by the Giri River. The area is home to a cluster of active faults. The Proterozoic age stromatolite-bearing dolomitic limestone (Srikantia and Sharma 1976; Thakur et al. 2010) encircles Sataun town on the north, while the Siwalik (Sub-Himalayan) Molassic deposits encircle the town on the south. Exposures of undifferentiated Subathu Paleogene rocks may be found southwest of Sataun. The

Lithotectonic border known as the MBT denotes the transition from the rocks of the Lesser Himalaya to the undifferentiated Subathu (Auden 1934).

3. Data and Methods

1.1 Data

Sentinel-1 unwrapped and geocoded interferograms, along with coherence data at a resolution of 0.001°, were generated using the LiCSAR system and made available through the COMET–LiCSAR web portal (COMET, 2020). The dataset consists of 2 LiCSAR frames, including 1 framefrom ascending orbits and 1from descending orbits, covering whole area of Sataun district during the observation period from October 2014 to mid of May 2024.The acquisition starts dates vary across frames due to the non-uniform observation strategy of Sentinel-1. For instance, the earliest data for frames 129A_05935_131313 and 136D_05854_131313 were collected on October26, 2014, and October 27, 2014, respectively. Additionally, some tracks and frames experienced significant data gaps during the observation period. Examples include a nearly year-long gap between June to august of 2015, 2016, 2018, 2019, and 2023in various times in 136D, similarly there is a huge a lack of data from June to November 2016, 2017, June-July 2018, March 2022 to October 2022, August 2023 to October 2023 in129A.

Most of the land is covered with forests in the study area. Dense vegetation prevents C-band SAR data from obtaining sufficient coherence in an interferogram, even with short temporal baselines (Rosen et al. 1996; Morishita et al. 2020), and tends to yield unwanted unwrapping errors. To avoid the impact of unwrapping errors and save the processing time and storage, this study focuses on urban areas.

1.2 Methods

LiCSBAS for the InSAR time series analysis was used in this work. This package has been run entirely on Python 3 and the Bourne Again Shell (Bash) the source code is available on the GitHub “yumorishita/LiCSBAS: LiCSBAS: InSAR time series analysis package using LiCSAR products.” https://github.com/yumorishita/LiCSBAS (accessed Jul. 02, 2023) The package also provides the InSAR data throughout the LiCSAR data-processing platform.

In this paper we have used different steps for downloading and processing the data. The workflow for InSAR time series analysis begins with the first steps which is Step 0: Preparation of Unwrapped Data. First, LiCSAR products relevant to the study area were downloaded (Step 0-1) and then converted into the required format (Step 0-2). Some added interferograms were used from the other satellites which were available and meet compatibility criteria like Terra SAR, then they were also processed with the data (Step 0-3). To enhance accuracy and efficiency, the unwrapped data undergo masking (Step 0-4) and were clipped to reduce processing loads (Step 0-5). Tropospheric noise correction was then applied using external data from the Generic Atmospheric Correction Online Service for InSAR (GACOS) (Step 0-6).

Thereafter, in the next major step which we used was Step 1: Time Series Analysis which begins by evaluating the coherence and coverage of the unwrapped data (Step 1-1). Thereafter loop closure check was performed to detect and remove any incorrectly unwrapped data (Step 1-2). The refined stack was then inverted to generate displacement time series and velocity (Step 1-3). Velocity standard deviation (STD) was then estimated (Step 1-4), and noisy pixels were masked using established noise indices (Step 1-5). A spatiotemporal filter was applied to minimize residual noise, resulting in filtered time series and velocity outputs (Step 1-6). (Fig. 2)
Finally, for the Output and Export stage, the processed results, including velocity and time series data, were exported in formats such as GeoTIFF, KMZ, and text files for further analysis and visualization.

The process of both the major steps, Step 0 and Step 1, was executed in the Virtual box Ubuntu 21.04 version via a batch script with predefined parameters and directly through the command line. LiCSBAS has offered a robust and streamlined solution for InSAR time series analysis, accommodating Sentinel-1 data as well as compatible interferograms from other satellite sources as informed in the earlier steps.

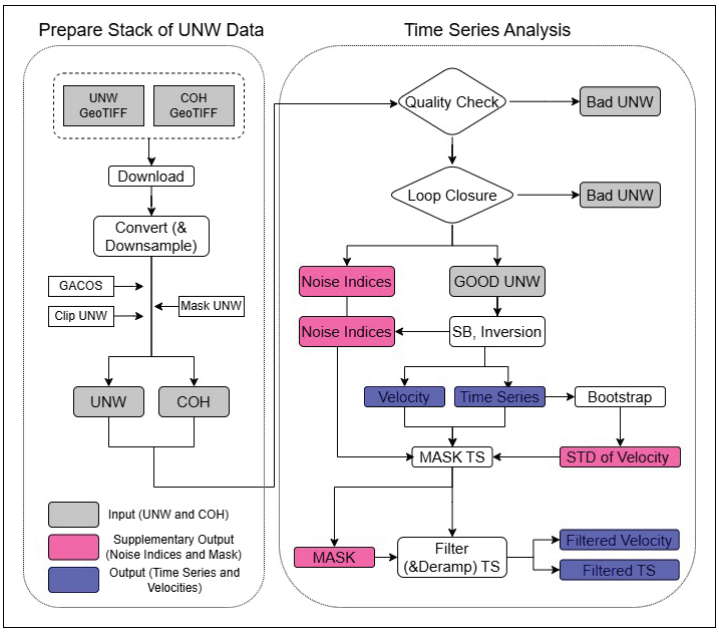


Fig2: The flow chart representing the method of the LiCSBAS preparation and time series analysis.

The tropospheric noise correction using the Generic Atmospheric Correction Online Service (GACOS) data (Yu C et al., 2018) was not applied in steps 0–3, This decision was made because the clipped areas was too small to disregard long-wavelength tropospheric noise, focusing instead on flat regions with minimal topography-correlated stratified tropospheric noise. To mitigate unwrapping errors in non-urban regions, pixels with an average coherence of d◂0.1 in the unwrapped data were masked in step 0–4 before proceeding with time series analysis. Subsequently, all unwrapped data and corresponding coherence images were clipped to predefined areas in step 0–5. The unwrapped coverage and coherence threshold for step 1–1 was set to 0.05 and 0.06, respectively. In step 1–5, strict thresholds were applied to mask noisy pixels based on several noise indices, ensuring the retention of reliable pixels. The small baseline (SB) network gap threshold was set to zero, ensuring a gap-free network and a robust time series. Thresholds for loop error, maximum connected time length, and interferograms without loops were set to 3, 3 years, and 10, respectively. The temporal filter width in steps 1–6 was set to 0.15 years (55 days), balancing the retention of seasonal deformation components with the sampling interval.

During the LiCSBAS processing, a primary stable reference point was automatically identified in steps 1–6. This was done by calculating the root mean square (RMS) of the cumulative deformation time series for each pixel, relative to the median deformation at each epoch. The pixel with the minimum RMS was selected as the stable reference point. For comparison or integration of results from multiple frames, a common reference point was set by averaging the RMS across all available frames and selecting the pixel with the lowest averaged RMS.

LiCSBAS technique was employed to analyze InSAR data for monitoring our study area and to process InSAR time-series data, enabling the detection and quantification of surface displacements linked to subsidence. The findings have provided valuable for supporting regional development planning, minimizing losses and casualties, and aiding in landslide hazard assessments and early warning systems. All the steps and result processing have been discussed in detail in the supplement document.

4. Results and Discussions

Most existing InSAR time series analysis tools, such as StaMPS or GIAnT, require users to generate interferograms for their area of interest. This process involves downloading a stack of Sentinel-1 SLC data and creating interferograms, which demands considerable time and disk space. LiCSBAS has offered a significant advantage by eliminating the need to create interferograms when LiCSAR products are available for the area of interest (Morishita

et al., 2020). This saves considerable time and storage. For instance, the Geo TIFF files for 300 interferograms occupy only about 5 GB in our study area, and the total file size generated by LiCSBAS for the Sirmaur test frames is approximately 30 GB.LiCSBAS output result gives for the frame 129A_05935_131313 and frame 136D_05854_131313. The result clearly indicates the velocity, loop, resid. In this paper we have seen the significant deformation in and around the landslide region which shows the movement of landslide.

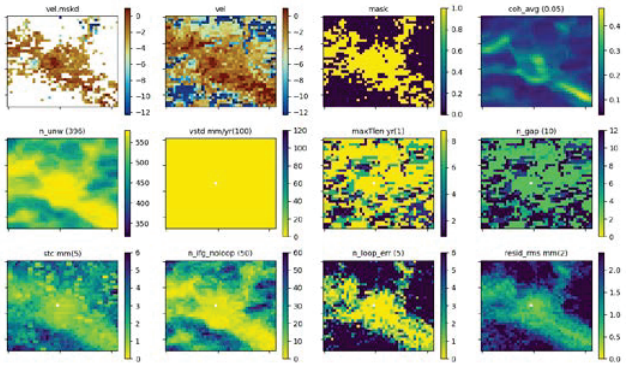


Fig 3: This figure shows the result for the frame 129A_05935_131313:the result shows the velocity masking in noisy pixels, derived from time-series analysis using a set of indices for the Sirmaur region. The top row displays both masked and unmasked velocities along with the applied mask, alongside the average coherence calculated from the input interferometric data. Additional images illustrate the various noise indices utilized in generating the mask, with their corresponding explanations and units detailed in Table 1. The threshold values applied to each noise index are indicated in parentheses beside their respective titles.

Table 1: List of the noise indices used for masking.

Noise index	**Meaning**
coh_avg	Average value of the interferometric coherence across the stack (0–1).
n_unw	Number of unwrapped data used in the time series calculation.
vstd	Standard deviation of the velocity (mm/yr) estimated in Step 1-4.
maxTlen	Maximum time length of the connected network (years). The larger the value, the better the precision in the velocity estimate (see **Section 3.5**).
n_gap	Number of gaps in the interferogram network and time series breaks.
stc	Spatiotemporal consistency (mm) [**55**], which is the minimum root mean square (RMS) of the double differences of the time series in space and time between the pixel of interest and an adjacent pixel among all adjacent pixels.
n_ifg_noloop	Number of interferograms with no loops that cannot be checked by the loop closure and possibly have unidentified unwrapping errors.
n_loop_err	Number of the unclosed loops after the network refinement in Step 1-2.
resid_rms	RMS of residuals in the small baseline (SB) inversion (mm).

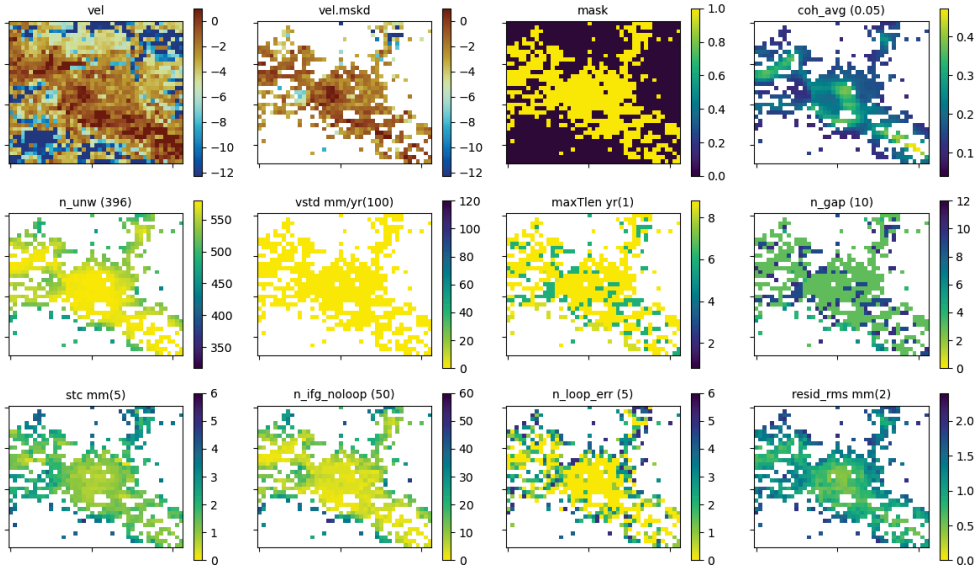


Fig 4: This figure shows the result for the frame 129A_05935_131313: the result shows after removal of the masked pixel, we can see the result of velocity masking in noisy pixels, derived from time-series analysis using a set of indices for the Sirmaur region. The top row displays both masked and unmasked velocities along with the applied mask, alongside the average coherence calculated from the input interferometric data. Additional images illustrate the various noise indices utilized in generating the mask, with their corresponding explanations and units detailed in Table 1. The threshold values applied to each noise index are indicated in parentheses beside their respective titles.

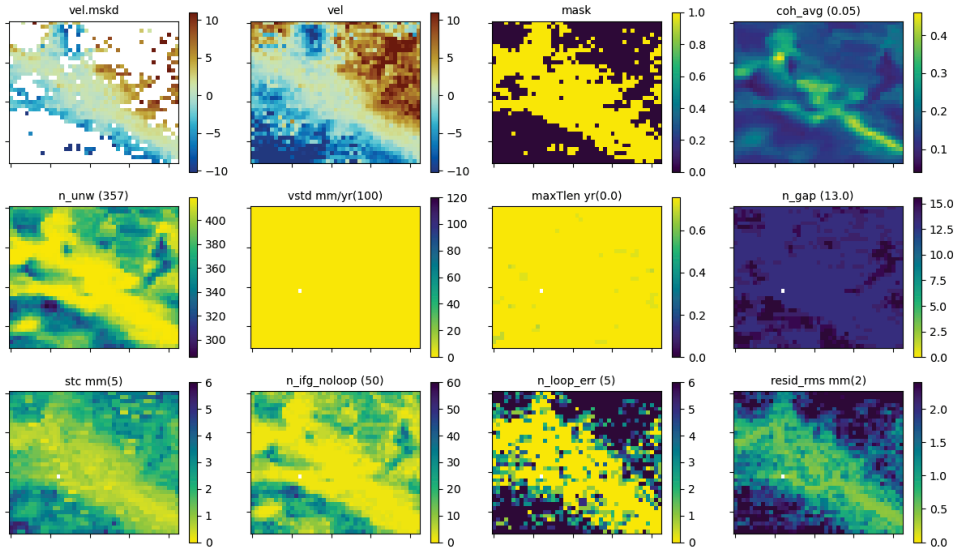


Fig 5: This figure shows the result for the frame 136D_05854_131313: this result also shows the velocity masking in noisy pixels, derived from time-series analysis using a set of indices for the Sirmaur region. The top row displays both masked and unmasked velocities along with the applied mask, alongside the average coherence calculated from the input interferometric data. Additional images illustrate the various noise indices utilized in generating the mask, with their corresponding explanations and units detailed in Table 1. The threshold values applied to each noise index are indicated in parentheses beside their respective titles.

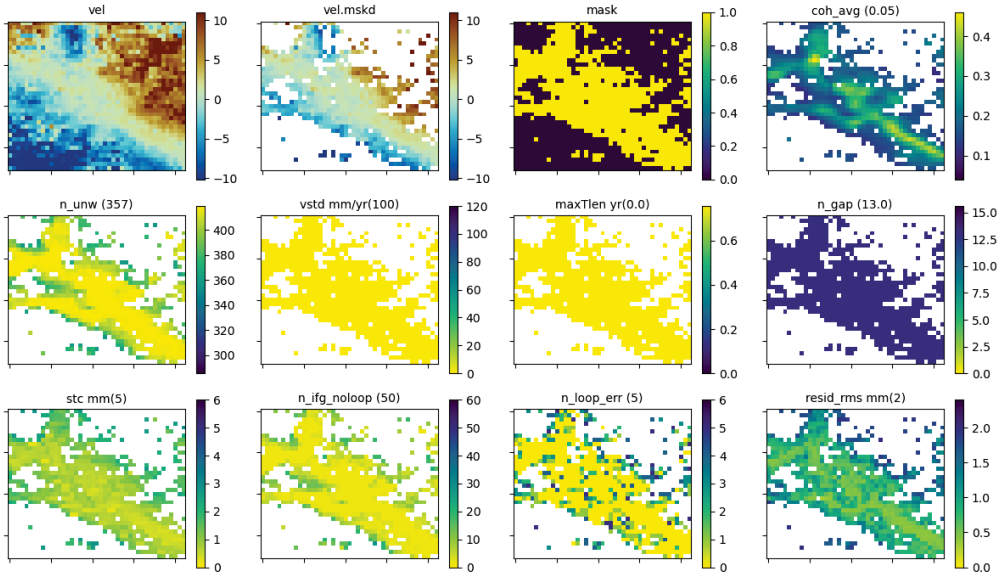


Fig 6: This figure shows the result for the frame 136D_05854_131313: the result shows after removal of the masked pixel, we can see the result of velocity masking in noisy pixels, derived from time-series analysis using a set of indices for the Sirmaur region. The top row displays both masked and unmasked velocities along with the applied mask, alongside the average coherence calculated from the input interferometric data. Additional images illustrate the various noise indices utilized in generating the mask, with their corresponding explanations and units detailed in Table 1. The threshold values applied to each noise index are indicated in parentheses beside their respective titles.

6. Limitations

The interferograms provided by LiCSAR are pre-processed with multi-looking to approximately 100 m (about 328.08 ft) resolution and subjected to strong spatial filtering. These adjustments align with the primary goal of the LiCS project: large-scale deformation monitoring and Landslide with small scale analysis has given a lot oferrors and gaps. While this approach excels at capturing regional deformations on the kilometer scale, however the regions less then this does not give good result, and show allots of errors in the study especially for the study of landslide as the vertical velocity calculation has shown errors.

To address gaps in the SB network, LiCSBAS applies a temporal constraint during the inversion stage (Step 1–3) this can be seen in the result folder of google drive. However, interpolated displacements in these gaps may not accurately reflect real-world deformations if they deviate from linear behavior. Assessing the uncertainty of the time series in such scenarios can be challenging, and potential biases should be carefully considered. The time series allowed us to easily identify gaps and improve interpretation.

7. Conclusions

LiCSBAS, an open-source InSAR time series analysis package, integrates seamlessly with outputs from the automated LiCSAR processing chain. By using pre-processed LiCSAR products, we bypass the need for generating interferograms from SLC data, thereby saving significant time and disk space. LiCSBAS has helped us to generate a loop closure test to automatically identify and exclude interferograms with extensive unwrapping errors, ensuring reliable time series and velocity estimations. Additional noise-based masking enhances result accuracy. This package's batch scripts with its simplified processing, and with customizing some parameters helped us to refine their results further. An interactive time series helps us to aid in interpreting displacement data.

Case study for the Sirmaur regions to study the landslide demonstrate that LiCSBAS's capability to detect both large-scale and localized deformations with sub-centimeter accuracy per epoch and velocity precision of ~2 mm/year. But the result might be as accurate as expected. However,further validating the result using the GNSS and leveling the data can confirm the findings, and the detection of linear, periodic, and episodic displacements in this region.

By eliminating the need to generate interferograms, LiCSBAS makes it easier to analyze Sentinel-1's globally available data, opening new opportunities for scientific exploration across diverse fields. This package has helped us to understand the slope stability using the InSAR in a much easier format.

Supplementary Materials

All the data for both the frames 129A_05935_131313 and 136D_05854_131313 is available in the folders with the frame names. Also, each frame has 2 main subfolders naming GEOCml1clip (contains the clipped interferograms for the interested regions for all the years); the TS_GEOCml1clip contains all results of velocity maps,deformation maps and other maps(Manocha, 2024). Similar folders with the same information are available for the other frame as well. All the steps of the methods have been discussed in detail in the supplement document.

8. REFERENCES

1. Agram, P.; Jolivet, R.; Simons, M. Generic InSAR Analysis Toolbox (GIAnT)—User Guide. Available online:http://earthdef.caltech.edu (accessed on 27 November 2019).
2. Agram, P.S.; Jolivet, R.; Riel, B.; Lin, Y.N.; Simons, M.; Hetland, E.; Doin, M.-P.; Lasserre, C. New Radar Interferometric Time Series Analysis Toolbox Released. Eos Trans. Am. Geophys. Union 2013, 94, 69–70.
3. Auden JB (1934) The geology of the Krol belt. Rec Geol Surv India 67(4):357–454
4. Avanzi GDA, Giannecchini R, Puccinelli A (2004) The influence of the geological and geomorphological settings on shallow landslides. An example in a temperate climate environment: the June 19, 1996, event in northwestern Tuscany (Italy). Eng Geol 73:215–228
5. Awasti SC (1966) Bulletin of Geological Survey of India 15(2):95–101
6. Bell JW, Amelung F, Ferretti A et al (2008) Permanent scatterer InSAR reveals seasonal and long-term aquifer-system response to groundwater pumping and artificial recharge. Water Resour Res 44. https://doi.org/10.1029/2007WR006152
7. Berardino P, Fornaro G, Lanari R, Sansosti E. (2002) "A new algorithm for surface deformation monitoring based on small baseline differential SAR interferograms". IEEE Transactions on Geoscience and Remote Sensing 40 (11): 2375–2383. Available from: https://doi.org/10.1109/tgrs.2002.803792
8. Bhambri R, Mehta M, Singh S, Jayangondaperumal R, Gupta A, Srivastava P (2013) Landslide inventory and damage assessment in the Bhagirathi Valley. Him Geol 38(2):193-205
9. Biggs, J.; Wright, T.; Lu, Z.; Parsons, B. Multi-interferogram method for measuring interseismic deformation: Denali Fault, Alaska. Geophys. J. Int. 2007, 170, 1165–1179.
10. Collins TK (2008) Debris flows caused by failure of fill slopes: early detection, warning and loss prevention. Landslides 5(1):107-120
11. COMET (2020) COMET-LiCS Sentinel-1 InSAR portal. https://comet.nerc.ac.uk/ COMET-LiCS-portal/. Accessed 24 June 2020
12. Das, I., Kumar, G., Stein, A., Bagchi, A., Dadhwal, V.K., 2011. Stochastic landslide vulnerability modeling in space and time in a part of the northern Himalayas, India. Environ Monit Assess 178, 25–37. https://doi.org/10.1007/s10661-010-1668-0
13. Dikshit A, Sarkar R, Pradhan B, Segoni S, Alamri AM (2020) Rainfall Induced Landslide Studies in Indian Himalayan Region: A Critical Review. Applied Sciences 10(7):2466. https://doi.org/10.3390/app10072466
14. Doin, M.-P.; Lodge, F.; Guillaso, S.; Jolivet, R.; Lasserre, C.; Ducret, G.; Grandin, R.; Pathier, E.; Pinel, V. Presentation of the small baseline NSBAS processing chain on a case example: The Etna deformation monitoring from 2003 to 2010 using Envisat data. In Proceedings of the Fringe 2011 Workshop, Frascati, Italy, 19–23 September 2011.
15. Efron, B.; Tibshirani, R. Bootstrap Methods for Standard Errors, Confidence Intervals, and Other Measures of Statistical Accuracy. Stat. Sci. 1986, 1, 54–75.
16. Evans SG, Roberts NJ, Ischuk A, Delaney KB, Morozova GS, Tutubalina O (2009) Landslides triggered by the 1949 Khait earthquake, Tajikistan, and associated loss of life. Eng Geol 109:195-212
17. Galve, J.; Pérez-Peña, J.; Azañón, J.; Closson, D.; Caló, F.; Reyes-Carmona, C.; Jabaloy, A.; Ruano, P.; Mateos, R.; Notti, D.; et al. Evaluation of the SBAS InSAR Service of the European Space Agency's Geohazard Exploitation Platform (GEP). Remote Sens. 2017, 9, 1291.

18. Guerriero L, Ruzza G, Maresca R, Guadagno FM, Revellino P (2021) Clay landslide movement triggered by artificial vibrations: new insights from monitoring data. Landslides 18(8):2949-57
19. Hoffmann, J.; Zebker, H.A.; Galloway, D.L.; Amelung, F. Seasonal subsidence and rebound in Las Vegas Valley, Nevada, observed by synthetic aperture radar interferometry. Water Resour. Res. 2001, 37, 1551–1566.
20. Homoud A, Tal AB, Taqieddin SA (1997) A comparative study of slope stability methods and mitigative design of a highway embankment landslide with a potential for deep seated sliding. Eng Geol 47:157-173
21. Hooper, A.; Segall, P.; Zebker, H. Persistent scatterer interferometric synthetic aperture radar for crustal deformation analysis, with application to Volcán Alcedo, Galápagos. J. Geophys. Res. Solid Earth 2007, 112, 1–21.
22. Hooper, A.J. A statistical-cost approach to unwrapping the phase of InSAR time series. In Proceedings of the Fringe 2009 Workshop, Frascati, Italy, 30 November–4 December 2009.
23. Hooper, A.J.; Bekaert, D.; Spaans, K.; Arikan, M. Recent advances in SAR interferometry time series analysis for measuring crustal deformation. Tectonophysics 2012, 514–517, 1–13.
24. Jain AK (2014) When did India–Asia collide and make the Himalaya?. Current Science 254-266
25. Karunakaran C, and Rao R (1979) Status of hydrocarbon in the Himalayan regions: contributions to stratigraphy and structure. Geol. Surv. India 41:1-66
26. Kothyari GC, Pant P, Luirei K (2012) Landslides and neotectonic activities in the main boundary thrust (MBT) zone: South-eastern Kumaon. J Geol Soc India 40:101-110
27. Lazecký M, Spaans K, González PJ et al (2020) LiCSAR: an automatic InSAR tool for measuring and monitoring tectonic and volcanic activity. Remote Sens 12: 2430. https://doi.org/10.3390/rs12152430
28. López-Quiroz, P.; Doin, M.P.; Tupin, F.; Briole, P.; Nicolas, J.M. Time series analysis of Mexico City subsidence constrained by radar interferometry. J. Appl. Geophys. 2009, 69, 1–15.
29. Manocha, Akshay (2024), "Landslide Deformation and Temporal Prediction (LDTP) using LiCSBAS in Himalayan Terrains.", Mendeley Data, V1, doi: 10.17632/mnkhct54vb.1
30. Medlicott HB (1864) On the geological structure and relations of the southern portion of the Himalayan ranges between rivers Ganges and the Ravi. Mem Geological Survey of India 3(2):122-122
31. Morishita Y, Lazecky M, Wright TJ et al (2020) LiCSBAS: an open-source InSAR time series analysis package integrated with the LiCSAR Automated Sentinel 1 InSAR Processor. Remote Sens 12:424. https://doi.org/10.3390/rs12030424
32. Morishita Y, Suzuki A, Amagai T et al (2010) Approach to efficient leveling by using InSAR (in Japanese). J Geospatial Inf Auth Japan 120:17–22
33. Paul SK, Bartarya SK, Routela P, Mahajan, AK (2000) Catastrophic mass movement of 1998 monsoons at Malpa in Kali Valley. Geomorphology 35:169-180
34. Powers PM, Lillie RJ, & Yeats RS (1998) Structure and shortening of the Kangra and Dehra Dun reentrants, sub-Himalaya, India. Geological Society of America Bulletin 110(8): 1010-1027
35. Raiverman V, Srivastava AK, Prasad DN (1994) Structural style in North western Himalayan foothills. Him Geol 15:263-280
36. Ray PKC, Parvaiz I, Jayangondaperumal R, Thakur VC, Dadhwal V, Bhat FA (2009) Analysis of seismicity-induced landslides due to the 8 October 2005 earthquake in Kashmir Himalaya. Curr Sci 97(12):1742-1751
37. Rosen PA, Hensley S, Zebker HA et al (1996) Surface deformation and coherence measurements of Kilauea Volcano, Hawaii, from SIR-C radar interferometry. J Geophys Res Planets 101:23109–23125. https://doi.org/10.1029/96JE01459
38. Schmidt DK, Bürgmann R. (2003) "Time-dependent land uplift and subsidence in the Santa Clara valley, California, from a large interferometric synthetic aperture radar data set". Journal of Geophysical Research: Solid Earth 108 (B9). Available from: https://doi.org/10.1029/2002jb002267
39. Singh J, Thakur M (2019) Landslide stability assessment along Panchkula–Morni Road, Nahan salient, NW Himalaya, India. Journal of Earth System Science128 (6):1-5
40. Singh J, Thakur M, Abhaypal GS, Kishore N (2022) Slope stability analysis of Strawberry Hill Landslide and adjoining slopes along National Highway-5, Shimla, Northwestern Himalaya, India. Arabian Journal of Geosciences. (11):1-5
41. Sorbino G, Nicotera MV (2013) Unsaturated soil mechanics in rainfall-induced flow landslides. Eng Geol 165:105-132
42. Srikantia SV and Bhargava ON (1998) Geology of Himachal Pradesh. GSI Publications, 2(1)
43. Srikantia SV, Sharma RP (1976) Tang C, Zhu J, Qi X, Ding J (2011) Landslides induced by the Wenchuan earthquake and the subsequent strong rainfall event: A case study in the Beichuan area of China. Eng Geol 122:22-33
44. Tang C, Zhu J, Qi X, Ding J. (2011) Landslides induced by the Wenchuan earthquake and the subsequent strong rainfall event: A case study in the Beichuan area of China. Engineering Geology 122(1-2):22-33
45. Thakur, M., Kumar, N., Dhiman, R. K., & Malik, J. N. (2023). Geological and geotechnical investigations of the Sataun landslide along the active Sirmauri Tal fault, Sataun, northwestern Himalaya, India. Landslides, 20(5), 1045-1063.
46. Wadia DN (1937) Permo carboniferous limestone inliers in the Sub Himalayan Tertiary zone of Jammu, Kashmir Himalaya. Records of the Geological Survey of India 72:162-173
47. Weiss, J.R.; Walters, R.J.; Morishita, Y.; Wright, T.J.; Lazecky, M.; Wang, H.; Hussain, E.; Hooper, A.J.; Elliott, J.R.; González, P.J.; et al. Plate-scale measurements of interseismic velocity and strain from Sentinel-1 InSAR and GNSS data. Manuscript in Preparation.

48. Yu C, Li Z, Penna NT, Crippa P. (2018) “Generic Atmospheric Correction model for interferometric synthetic aperture radar observations”. Journal of Geophysical Research: Solid Earth 123 (10): 9202–9222. Available from: https://doi.org/10.1029/2017jb015305
49. Yunjun Z, Fattahi H, Amelung F. (2019) “Small baseline InSAR time series analysis: Unwrapping error correction and noise reduction”. Computers & Geosciences 133:104331.